Nanoscale

PAPER

View Article Online
View Journal | View Issue

Published on 25 September 2015. Downloaded by Pennsylvania State University on 16/09/2016 06:11:00.

Cite this: *Nanoscale*, 2015, **7**, 18105

Investigation of the size–property relationship in $CuInS_2$ quantum dots†

T. Akdas,[a] J. Walter,[a] D. Segets,[a] M. Distaso,[a] B. Winter,[b] B. Birajdar,‡[b] E. Spiecker[b] and W. Peukert*[a]

Received 27th June 2015,
Accepted 19th September 2015

DOI: 10.1039/c5nr04291g

www.rsc.org/nanoscale

In this work we investigated fundamental properties of $CuInS_2$ quantum dots in dependence of the particle size distribution (PSD). Size-selective precipitation (SSP) with acetone as poor solvent was performed as an adequate post-processing step. Our results provide deep insight into the correlation between particle size and various optical characteristics as bandgap energy, absorption and emission features and the broadness of the emission signal. These structure–property relationships are only achieved due to the unique combination of different analytical techniques. Our study reveals that the removal of 10 wt% of smallest particles from the feed results in an enhancement of the emission signal. This improvement is ascribed to a decreased quenching of the emission in larger particles. Our results reveal the impact of PSDs on the properties and the performance of an ensemble of multicomponent QDs and anticipate the high potential of controlling PSDs by well-developed post-processing.

1. Introduction

The study of nanometer sized crystals is an interesting and ongoing research field for more than thirty years. Considerable progress has been made in the synthesis and understanding of metals[1–6] and semiconductor nanocrystals.[5,7–9] The latter, and amongst them especially CdS(e), CdTe and PbS(e), have often served as technically relevant model systems to understand property changes due to quantum confinement. However, for real life applications less toxic semiconductors have to be investigated as alternatives to Cd- and Pb-based binary nanocrystals.[10] With its direct bandgap of 1.53 eV[11] and a high absorption coefficient (10^4–10^5),[12,13] $CuInS_2$ is an ideal candidate for solar cell applications.

For optimum device performance, it is necessary to accurately adjust the mean size and also the PSD of the particles.[14–16] Control of synthesis parameters is a key factor to obtain desired properties. However, as nucleation, growth and ripening superimpose with each other, limitations are observed. Therefore, post-processing steps are necessary to narrow the PSD. Possible techniques for size fractionation are gel electrophoresis,[17,18] exclusion chromatography,[19] reversed micelle preparation,[20] size-selective precipitation (SSP)[21–23] or flow-field fractionation (FFF).[24–26] Detailed summaries of techniques used for separation of nanoparticles by their size and/or shape are provided in reviews by Kowalczyk[27] and Mori.[28]

For $CuInS_2$ nanocrystals, a broad absorbance spectrum without a well pronounced peak but with a long tail to lower energies was observed by several groups.[29–31] In both absorbance and emission spectra, two or even three peaks have been identified: while the positions of these peaks were not changing significantly, their intensity and ratio were often dependent on synthesis time and storage atmosphere.[29] These observations could be the result of several factors, namely, a wide size distribution, electron density leakage from the core of the crystals into the ligand layer and/or intra-bandgap states.[29] However, a final conclusion on the habit of $CuInS_2$ nanocrystals is still missing.

In the present paper, a detailed study of the PSD of $CuInS_2$ quantum dots (QDs) and its influence on the optical characteristics is presented. Thereby, we attempt to distinguish between properties that are inherently related to the dispersity of $CuInS_2$ below 6 nm and those associated with unwanted variations in sample quality, *e.g.* irregular distributions in composition. SSP which was chosen due to its scalability and its potential applicability within a continuous process was performed to classify the nanocrystals into three different fractions, namely coarse, fines and residuals fraction. Prior to classification, a detailed characterization of the feed material was carried out by transmission electron microscopy (TEM),

[a]*Institute of Particle Technology (LFG), Friedrich-Alexander-Universität Erlangen-Nürnberg (FAU), Cauerstr. 4, 91058 Erlangen, Germany.*
E-mail: wolfgang.peukert@fau.de
[b]*Center for Nanoanalysis and Electron Microscopy (CENEM), Friedrich-Alexander-Universität Erlangen-Nürnberg (FAU), Cauerstr. 6, 91058 Erlangen, Germany*
†Electronic supplementary information (ESI) available: A scheme on the process, graphics and data on reproducibility are given in the ESI together with additional experiments and their discussion. See DOI: 10.1039/c5nr04291g
‡Present address: Special Centre for Nanoanalysis, Jawaharlal Nehru University, New Delhi-110067, India.

Published on 25 September 2015. Downloaded by Pennsylvania State University on 16/09/2016 06:11:00.

analytical ultracentrifugation (AUC) and optical spectroscopy. Absorbance spectra were converted into PSDs by a previously described deconvolution technique that has been successfully applied to ZnO,[32] PbS(e)[33] and ZnS[34] QDs. The crystal structure and composition of the feed as well as the isolated fractions after classification were investigated by X-ray diffraction (XRD), thermogravimetric analysis (TGA) and inductively-coupled plasma optical emission spectroscopy (ICP-OES). Our results reveal that the observed optical properties of a $CuInS_2$ QD batch can be attributed to the different size fractions of the PSD after synthesis and are not caused by unwanted particles with wrong composition.

2. Experimental

2.1. Chemicals

All chemicals were used as received and without further purification. Copper(I) acetate (CuAc, 97%), indium(III) acetate (In $(Ac)_3$, 99.999%), 1-octadecene (1-ODE, 95%) and 1-dodecanethiol (1-DDT, ≥98%) were obtained from Aldrich. CuAc and $InAc_3$ were stored in a nitrogen-filled glovebox to prevent degradation. Toluene (99.5%) was obtained from Acros. Acetone (≥99.8%) and chloroform ($CHCl_3$, ≥99%) were obtained from Roth, Rhodamin 6G (Rho6G, 95%) was purchased from Sigma Aldrich.

2.2. Synthesis of $CuInS_2$ nanocrystals

Synthesis was carried out using a Schlenk line. A 50 ml round three-necked bottom flask was placed in a heating mantle. One neck was connected to a condenser and the other sealed by a septum. A thermocouple was used to provide accurate temperature control. 1-ODE was degassed minimum 30 minutes prior to synthesis. CuAc (81 mg, 0.66 mmol), $InAc_3$ (193 mg, 0.66 mmol), 1-DDT (1.5 ml, 6.3 mmol) and 1-ODE (14 ml) were added into the flask, degassed by pulling vacuum for 10 minutes, followed by N_2 bubbling for one minute. This procedure was repeated three times. Afterwards, the mixture was heated to 240 °C. The reaction was carried out for one hour and then the reaction vessel was quickly cooled down to room temperature by using a water bath.

2.3. Purification of $CuInS_2$ nanocrystals

Purification of the nanocrystals was conducted by first adding one equivalent $CHCl_3$ to the reaction solution, followed by the addition of one equivalent of acetic acid and three equivalents of acetone as antisolvent to flocculate the nanocrystals.[35] Centrifugation was carried out for 10 minutes at 8240*g*. The supernatant was discarded and the obtained precipitate was redispersed in $CHCl_3$. This cycle was repeated five times in total. The final product was dried at room temperature and can be redispersed in any lipophilic solvent, such as toluene, hexanes or chloroform.

2.4. Size-selective precipitation experiments for size focusing

Purified and dried $CuInS_2$ QDs (reddish waxy powder, feed) were redispersed in 4 ml toluene. One equivalent of acetone was added to flocculate the nanocrystals, followed by ultrasonication for 5 minutes and centrifugation at 8240*g* for 10 minutes. The flocculates were separated from the supernatant and dried at ambient atmosphere overnight. One further equivalent (total of two equivalents, 8 ml) of antisolvent was added to the supernatant and the centrifugation step was repeated. After eight cycles of separation (32 ml of acetone added in total), the solvent of the still slightly colored supernatant was evaporated and the dried sample was weighed and kept for further analysis. The samples after each centrifugation step were categorized into a coarse fraction *c* (centrifugation steps 1–4) and a fines fraction *f* (centrifugation steps 5–8), dependent on their absorption behavior. The particles that could not be separated by centrifugation were categorized as residuals fraction *r*. An overview of the masses of the feeds and all fractions together with mean values and standard deviations for the three single exemplary experiments are given in Table S1 in the ESI.† Calculation of the relative masses of these fractions was performed according to following eqn (1)–(3). They relate the isolated mass of the coarse m_c (fraction #1), the fines m_f (fraction #2) and the residuals fraction m_r (fraction #3) to the mass of the feed m_{tot}:

$$c = \frac{m_c}{m_{tot}} \quad (1)$$

$$f = \frac{m_f}{m_{tot}} \quad (2)$$

$$r = \frac{m_r}{m_{tot}} \quad (3)$$

2.5. Materials characterization

All nanocrystals were characterized using a range of analytical techniques introduced below. The reproducibility of the experiments was checked by performing the same experiments from various batches. A high purity and cleanliness is necessary for successful SSP. Mean values and standard deviations were obtained from at least three experiments for the feed and fraction #1 and two experiments for fractions #2 and #3. This is inherent to the experiments due to less material available for fractions #2 and #3 while a high amount of material is needed to conduct all characterizations.

2.5.1. Transmission electron microscopy (TEM). High-resolution (HR) TEM was performed with an image-side aberration corrected FEI Titan^3 80-300 TEM operated at 200 kV. All HRTEM micrographs were obtained at a reduced spherical aberration (Cs < 10 micrometers) and minimum contrast of the support film. The electron beam irradiation of the imaged area was minimized to avoid ripening of the nanoparticles. To prevent agglomeration, the nanoparticle dispersions in chloroform solution were put in an ultrasonic bath for 2 minutes and were then drop casted onto TEM sample grids with ultrathin carbon films supported by a lacey carbon film (Ted Pella

 This journal is © The Royal Society of Chemistry 2015

Published on 25 September 2015. Downloaded by Pennsylvania State University on 16/09/2016 06:11:00.

Inc. USA). Selected area electron diffraction (SAED) was performed using a Philips CM30 TEM operated at 300 kV and a FEI Titan^3 80-300 TEM operated at 200 kV. The particle sizes were determined by applying the Scherrer equation (as explained below) to rotationally averaged SAED ring patterns. The wavelengths of electrons with energies of 200 keV (λ = 2.51 pm) and 300 keV (λ = 1.97 pm) were used.

2.5.2. X-Ray diffraction (XRD). XRD analyses in Bragg-Brentano geometry were performed with a Bruker AXS Advance D8 (Karlsruhe, Germany) instrument using Cu K_α radiation ($\lambda_{K\alpha}$ = 1.54 Å) at an acceleration voltage of 30 kV and 40 kV. The XRD patterns were measured in the 2θ range between 10° and 80° with a step size of 0.02°. The diffractometer was equipped with a 1-dimensional Vantec-1 high-speed detector and a rotating sample stage. Low background sample cups with a vicinal (911) Si crystal of 25 mm diameter were purchased from Bruker AXS and used as substrates for the XRD scans. All samples were prepared by drop-casting the dispersion onto the substrate followed by evaporation of the solvent. The coherence lengths L_{hkl} along the different crystal directions were calculated from the full width at half maximum (FWHM) of the diffraction peaks by using the Scherrer equation and assuming Gaussian shaped peaks:

$$T = \frac{K\lambda}{\beta \cos \theta} \quad (4)$$

where T is the mean crystallite size, K is a dimensionless shape factor (here: 0.9), λ is the wavelength of the X-ray ($\lambda_{K\alpha}$ = 1.54 Å), β is the line broadening at FWHM and θ is the Bragg angle.

2.5.3. Thermogravimetry (TG). TG analyses were performed on a TGA Q50 from TA Instruments. Masses of around 15 mg dried powder samples were heated up to 500 °C in a platinum pan under a constant nitrogen flow of 40 ml min^{-1}, with a heating rate of 10 K min^{-1}. TA Instrument Analysis Software was used to analyse and export the data.

2.5.4. Inductively coupled plasma optical emission spectroscopy (ICP-OES). Dried powder samples were digested using aqua regia (4 ml) and diluted with millipore water. Analyses were performed with an ICP-OES Spectrometer Optima8300 from Perkin Elmer.

2.5.5. Analytical ultracentrifugation (AUC). A modified preparative centrifuge, type Optima L-90 K from Beckman Coulter, was used to perform sedimentation velocity experiments. Detailed information regarding the applied Ocean-Optics UV/Vis detector (USB2000+) as well as the data acquisition can be found in the literature.[36,37] Two-sector titanium centerpieces from Nanolytics, Germany, with a path length of 12 mm were used for all experiments. Samples were diluted up to equal absorbance of ~0.7 at 350 nm in the AUC cell. The solvent density was 0.8622 g cm^{-3} and the solvent viscosity was 0.553 mPas. The core density of bulk $CuInS_2$ [38] was 4.739 g cm^{-3}. Sedimentation velocity data were acquired every two minutes at 25 000 rpm, 25 °C and a radial resolution of 50 μm. Multiwavelength intensity data were recorded from 300 to 600 nm. The sedimentation coefficients s and diffusion coefficients D of the QDs become accessible through Lamm's equation and are linked to the particle diameter and density through Stokes' and Einstein's laws. Further information regarding the theoretical background of AUC is provided in the ESI.†

For our studies, intensity data at 360 nm was converted to absorbance data and was evaluated with Sedfit (Version 14.6e) using the $c(s,D)$ and $c(s)$ models.[39–41] For the $c(s,D)$ analysis, data were fitted with a second derivative regularization using confidence levels (F-ratios) of 0.683 for s and 0.9 for D. A resolution of 30 grid points in s and 30 grid points in D resulting in 900 grid points in total was used. For the $c(s)$ analysis, data were fitted with a second derivative regularization using a confidence level (F-ratios) of 0.9 and a resolution of 100 grid points. The best-fit partial specific volumes obtained by the $c(s,D)$ analysis were taken for the $c(s)$ analysis. Time-independent and radial invariant noise fitting was enabled for all evaluations. The parameters obtained by the core–shell model were taken to derive the core PSDs from the $c(s)$ distributions which were then used for the bandgap correlation.

2.5.6. Optical characterization. Absorbance spectra were recorded using a Perkin Elmer Lambda35 spectrometer. Quartz glass cuvettes with an optical path length of 10 mm were used for all measurements. For all absorption measurements, the powders were redispersed in toluene and their optical density was set to 0.1 at a wavelength of 480 nm. Emission spectra were collected on a Fluorolog Horiba Jobin Yvon. The sample in toluene was excited at λ_{exc} = 480 nm and emission spectra were recorded from 500 nm to 850 nm.

PSDs were determined from absorbance spectra according to Segets *et al.*[32–34] In its current form, the method is based on a linear superposition of the different particle size fractions, an assumption which has been already reported by various groups[42–45] in the literature. For the $CuInS_2$ nanoparticles of this study we used a bulk bandgap of 1.53 eV[11] and a bulk absorption according to Alonso *et al.*[46]

The bandgap *vs.* particle size relationship $\Delta E(x)$ was derived by an internal calibration of the absorbance results against AUC data. In brief, $\Delta E(x)$ was varied until a best match between PSDs from absorbance (PSD^{alg}) and target PSDs from AUC (PSD^{AUC}) was obtained. A similar procedure was already proposed by Mićić *et al.*[45] on InP QDs and more recently applied by Segets *et al.*[33] on PbS(e) QDs. Noteworthy, the latter led to an excellent agreement with literature data on $\Delta E(x)$ showing the high potential of this approach. Analogue to that previous study on PbS(e), a power law with three empiric parameters a [nm], b [–] and c [nm] was used to describe the correlation between particle size and bandgap energy according to eqn (5):

$$x(\Delta E) = a\left(\frac{\Delta E - E_{g,bulk}}{eV}\right)^b + c \quad (5)$$

with x being the particle size, ΔE the increase in bandgap energy due to quantum confinement and $E_{g,bulk}$ being the bulk bandgap (1.53 eV).[11] Within the deconvolution algorithm,

Published on 25 September 2015. Downloaded by Pennsylvania State University on 16/09/2016 06:11:00.

parameters a, b and c were varied until a best match of $PSDs^{alg}$ with the $PSDs^{AUC}$ of fraction #1 and #2 was obtained. As found in previous work, only two fractions are necessary to cover a larger particle size range. This leads to values of a, b and c and results in a function for $\Delta E(x)$ that is valid over a wide size region. Due to the fact that the shape of the distributions derived from AUC and absorbance data is substantially different (reasons will be discussed later), special emphasis during the matching procedure was given to the consistent size range of $PSDs^{alg}$ in comparison to $PSDs^{AUC}$. After having determined the empiric parameters to be a = 2.0301 nm, b = −0.649 and c = 0 nm, eqn (5) can be rearranged as follows in order to plot the bandgap *vs.* size dependency.

$$\Delta E = E_{g,bulk} + \left(\frac{x-c}{a}\right)^{\frac{1}{b}} \text{ eV} \quad (6)$$

3. Results and discussion

3.1. Characterization of as-synthesized particles

$CuInS_2$ QDs were synthesized similar to an established one-pot procedure which utilizes 1-DDT as sulfur source and stabilizer.[47] In accordance with the literature, broad absorbance and emission spectra that are composed of several features were observed. In previous works,[29–31] it was stated that a SSP led to none or just slight differences in the spectra of the isolated individual fractions. However, the resulting spectra and separated fractions were neither analyzed in terms of their PSDs nor in terms of their emission properties.

A first qualitative examination of the size range possibly present in an as-synthesized sample was performed using HRTEM and SAED investigations. Fig. 1a shows an overview HRTEM image of the $CuInS_2$ nanocrystals that had been dispersed onto a thin carbon film (amorphous contrast). The QDs are crystalline particles in a size range roughly between 1 and 4 nm. Bigger and smaller particles are usually found adjacent to each other. However, regions consisting primarily of only smaller particles or of only bigger particles were also occasionally observed. Fig. 1b shows a SAED ring pattern of a region with smaller particles which can as well be seen in the HRTEM images. The diffraction rings are rather broad due to the small crystallite size, the $\{112\}_{CuInS_2}$ ring is even hard to identify. An analysis of the $\{204\}_{CuInS_2}/\{220\}_{CuInS_2}$ rings using the Scherrer equation results in a mean crystal size of about 1.4 nm. This value is in agreement with respective HRTEM images. Fig. 1c shows SAED and HRTEM measurements from a region with bigger particles. The SAED measurements confirm the expected tetragonal $CuInS_2$ crystal structure (see Fig. 1c). The rings are narrower and the analysis of the $\{112\}_{CuInS_2}$ ring using the Scherrer equation results in a mean crystal size of 3.0 nm which is as well in accordance with the corresponding HRTEM image. A determination of the exact PSD *via* HRTEM is challenging due to various reasons, *e.g.* carbon contaminations, ripening of the nanocrystals, and

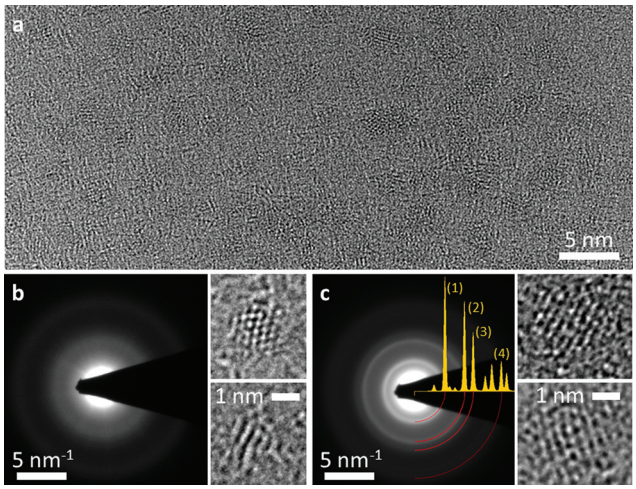

Fig. 1 (a) HRTEM overview image of $CuInS_2$ QDs on a carbon supported film, (b) SAED pattern and HRTEM images from a region with smaller particles, (c) SAED pattern and HRTEM images from a region with larger particles – the theoretically expected position (red ring fragments) and intensity distribution (yellow graph) of the SAED ring pattern of $CuInS_2$ nanocrystals are indicated. The four predominant ring intensities belong to the {112} (1), {204}/{220} (2), {116}/{312} (3) and {228}/{424} (4) lattice planes of tetragonal $CuInS_2$ [ICSD no. 186714].

underdetermination of nanocrystals smaller than 1.5 nm.[34,46] Especially in the case of multicomponent nanocrystals as $CuInS_2$, the low contrast between the imaged nanocrystals and the amorphous background is severely hindering an accurate evaluation.

Summarizing, the HRTEM and SAED results show solely $CuInS_2$ QDs with a tetragonal crystal structure and diameters ranging approximately from 1.4 nm to 3 nm. Considering the existence of a PSD in the sample, SSP was attempted with the goal to examine size–property relationships of $CuInS_2$ QDs. Before focusing on the optical properties, the structure and composition of each fraction was analyzed. This was necessary to make sure that no detectable side-products or unwanted particles with wrong composition cause a misinterpretation of the results.

3.2. Classification of $CuInS_2$ quantum dots

SSP is performed by stepwise addition of an antisolvent to a dispersion of nanocrystals in a good solvent inducing flocculation. The formed flocculates are then easily separated from the supernatant by centrifugation.[21,23] Usually, larger particles flocculate first, leading to a classification effect. By a stepwise increase of the amount of antisolvent and by repeating the aforementioned steps, the different size fractions can be extracted from the mixture. In Scheme S1 in the ESI† the SSP procedure applied herein is illustrated. Hydrophobic toluene was used as good solvent in which the nanocrystals are well-dispersed, whereas hydrophilic acetone was chosen as poor solvent to induce flocculation of the particles. By stepwise increasing the added amount of acetone, it was attempted to isolate largest particles which most probably lead to the

 This journal is © The Royal Society of Chemistry 2015

Published on 25 September 2015. Downloaded by Pennsylvania State University on 16/09/2016 06:11:00.

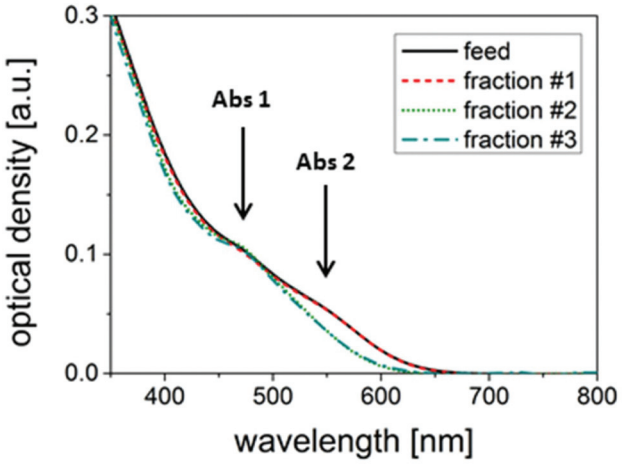

Fig. 2 Absorption spectra of the feed (black line), coarse fraction #1 (red dashed line), fines fraction #2 (green dotted line) and residuals fraction #3 (cyan blue dashed-dotted line). The two features Abs 1 and Abs 2 that are relevant in the following are highlighted by black arrows.

absorption feature at longer wavelengths. However, the addition of up to five equivalents of acetone was necessary to recognize a valuable change in the absorption spectrum (the spectra are shown in Fig. 2, discussion and analysis of the spectra will follow in section 3.5). Therefore, all nanocrystals separated by adding up to four equivalents of acetone were combined after flocculation, redispersion and analysis and are belonging to coarse fraction #1. Further addition of up to eight equivalents of acetone led to fines fraction #2. The supernatant after removal of these two fractions was still slightly colored, indicating the existence of dispersed primary nanoparticles. In order to access these residual nanocrystals, the supernatant was kept and the solvent was evaporated at room temperature. This led to the residuals fraction #3. Note that the amount of added antisolvent necessary to recognize changes in the spectra might vary depending on the particle sizes in the feed and, thus, depending on the overall PSD. The relative masses c, f and r for the coarse (#1), the fines (#2) and the residuals (#3) fractions, respectively, were determined from the masses of the dried powders according to eqn (1) to (3) (see Experimental part). Thereby, c was calculated to be 0.90 (±0.013), f was determined to be 0.04 (±0.018) and r was found to be 0.02 (±0.007). A small mass fraction of 0.04 (±0.023) is missing (Table S1, ESI†) which is mainly ascribed to losses at walls of centrifugation tubes, *e.g.* during decantation after each cycle. A more detailed discussion of the mass balance will follow in section 3.5.

3.3. Structure and composition of $CuInS_2$ QDs and their ligand shell after SSP

To verify the crystal structure and the composition of the three single fractions (coarse #1, fines #2, residuals #3), XRD and ICP-OES were performed. In Fig. S1a† the diffraction patterns are shown, Table 1 summarizes the mean particle sizes calculated by using the Scherrer formula. For the feed, coarse fraction #1 and fines fraction #2, the same three diffraction patterns were present. They can be assigned to the main diffractions (112), (204) and (312) of the tetragonal roquesite structure.[48] The mean particle sizes are 2.9 nm for the feed, 2.8 nm for the coarse and 2.4 nm for the fines fraction. No further diffractions or irregularities were observed in the feed, coarse fraction #1 or fines fraction #2. All spectra confirm the existence of a product with tetragonal crystal structure for all fractions. This is in accordance with HRTEM and SAED results shown in Fig. 1 where no additional phases throughout the entire feed were detected. In contrast to that, the residuals fraction #3 is showing irregularities. The diffraction pattern in this case is very diffuse with two very broad signals that are not interpretable. To analyze this behavior of residuals fraction #3 further, TG analyses were performed.

In Fig. S1b,† TGA results are shown and the relative mass losses are summarized in Table 1. The feed sample shows a decrease of 45.5 wt% at around 300 °C. At this temperature long-chained organic ligands are evaporated. A similar curve is obtained for the coarse fraction #1 with a total mass loss of 45.6 wt%. For fines fraction #2, a different behavior was observed. While a slightly enhanced main mass loss was still observed at 300 °C (46.8 wt%), an additional mass removal of ~8 wt% was detected at moderate temperatures between 150 °C and 250 °C. The detection of a slightly increased mass loss at 300 °C is not astonishing as we expect the ligand coverage not to change much with varying core size.[49] Due to the higher surface-to-volume ratio of smaller particles in fraction #2, the sample provides more surface area and thus must show a higher relative amount of organics compared to the feed and coarse fraction #1. The evaporation of compounds at relatively

Table 1 Summary of the data derived from structural and compositional analysis of the feed sample, the coarse fraction #1, the fines fraction #2 and the residuals fraction #3. The TGA values for feed and fraction #1 were obtained from at least three separate experiments, those for fraction #2 and #3 were obtained from two separate experiments

	Atomic composition (ICP-OES)				
Sample	Cu [at %]	In [at %]	S [at %]	Mean crystallite size (XRD) [nm]	Relative weight loss (TGA) [wt%]
Feed	1.0	1.2 ± 0.02	1.9 ± 0.07	2.8 ± 0.1	45.5 ± 0.3
Fraction #1	1.0	1.1 ± 0.02	2.1 ± 0.12	2.8 ± 0.1	45.6 ± 0.3
Fraction #2	1.0	1.1 ± 0.01	1.9 ± 0.10	2.4 ± 0.1	53.3 ± 1.3
Fraction #3	1.0	1.2 ± 0.06	2.3 ± 0.56	—	82.4 ± 6.8

Published on 25 September 2015. Downloaded by Pennsylvania State University on 16/09/2016 06:11:00.

low temperatures, however, hints on the existence of additional loosely-bound molecules that cannot be unambiguously explained for the time being. Most probably, these could be excess ligands or (anti)solvents such as toluene or acetone. Furthermore, residuals fraction #3 was analysed. The TGA curve with a total mass loss of 87.3 wt% shows that this fraction mainly consists of organic components. This result explains the observations for fraction #3 in XRD, where no distinct diffraction pattern was obtained.

Additional to XRD and TGA, ICP-OES was performed to check the composition of the particles within the isolated fractions after dissolution of the solid by aqua regia. The results are summarized in Table 1. The compositions in the single fractions are almost identical with Cu : In ratios of 1 : 1.1 (slight indium excess) and Cu : S of 1 : 2. Therefore, they prove the existence of stoichiometric $CuInS_2$ QDs over the entire size range. Concerning the mean Cu : S ratios, the highest sulfur amount was detected for fraction #3. Removal of sulfur containing organic molecules from the QDs in the single centrifugation steps results in an enrichment of these molecules in the supernatant. After evaporation of the supernatant these molecules are left in the sample (fraction #3).

Concluding, the results from XRD, TGA and ICP-OES together with the observations from HRTEM and SAED reveal that the particle cores of feed, #1 and #2 are homogeneous in composition and crystal structure over the entire size range within the detection limits of the devices. Regarding the residuals fraction #3, our results from ICP-OES and TGA together with HRTEM suggest $CuInS_2$ cores as well which are covered by a very high amount of organic molecules.

3.4. Investigation of the fractions *via* analytical ultracentrifugation

The ability of AUC to precisely characterize QDs *via* sedimentation velocity experiments was shown numerous times in literature.[37,49,50] Hence, AUC measurements were carried out to investigate the hydrodynamic properties of the different fractions obtained by SSP which are accessible *via* the sedimentation coefficient distributions. The sedimentation coefficient provides the sedimentation velocity of a particle divided by the centrifugal acceleration in the AUC. It can be converted to the particles size according to Stokes' equation (eqn (S3) in ESI†). However, for small particles the hydrodynamic properties will strongly depend not only on the core size but also on the shell morphology, *e.g.*, shell thickness and shell density. Therefore, it is not possible to calculate the particle size without knowing the particle density. A possibility to determine the particle size and density in just one AUC experiment is the multidimensional approach of simultaneously fitting the sedimentation and diffusion coefficients.[51,52] For this, the frictional ratio which is the hydrodynamic diameter divided by the volume equivalent diameter has to be equal 1. For the $CuInS_2$ QDs investigated in this study this is a fair assumption since they are spherical in good approximation as shown by the TEM data of Fig. 1. Herein, we performed a 2-dimensional analysis on all samples using the $c(s,D)$ analysis, which provided us with the sedimentation and diffusion coefficient distributions for all species (see Fig. S2 in ESI†).

Noteworthy, the reproducibility of the synthesis and subsequent AUC analytics was found to be excellent with only a few percent deviation between both measurement series. For all species we calculated the mean particle size and the particle density based on the peak positions in the 2-dimensional evaluation (Table 2). It becomes clear that the distributions of the feed and fraction #1 are very similar with a mean peak maximum of 11.35 sved for the feed and 10.78 sved for fraction #1. In contrast, fraction #2 reveals a second main species at 6.96 sved, which was not observable in the feed before. This can be explained by the strong enrichment of this smaller species in fraction #2 during SSP. For fraction #3, a much faster sedimenting species is found. The large sedimentation and low diffusion coefficient indicate that this species resembles aggregates of smaller primary particles linked by organic molecules. A higher deviation was also found for this fraction due to the random structure of the agglomerates.

Mean hydrodynamic diameters x_h of 4.38 nm, 4.44 nm and 3.75 nm are found for the feed, fraction #1 and fraction #2, respectively. A much larger hydrodynamic diameter of 13.65 nm is found for fraction #3 due to its aggregated structure. The mean particle density of the feed was derived to be 1.453 g cm^{-3} *via* the 2-dimensional evaluation. The density further decreases for fractions #1 (1.407 g cm^{-3}) and fraction #2 (1.355 g cm^{-3}) due to the increasing relative contribution of the less dense shell to the total particle density.

In the next step, we calculated the core diameters x_c and ligand shell thicknesses d_{shell} for the feed and fractions #1 and #2 based on a mass conservation approach presented by Carney *et al.*[51] The results in Table 2 show that d_{shell} was found to be about 1 nm for feed and coarse fraction #1 whereas a slightly smaller value of 0.92 nm was obtained for fraction #2.

Table 2 Summary of the data derived from the 2-dimensional AUC analysis of the feed sample, the coarse fraction #1, the fines fraction #2 as well as the residuals fraction #3. Values were taken using the peak maxima of the main fractions. A second independent synthesis and AUC measurement was carried out to calculate mean parameters and standard deviations

Sample	s [sved]	D [10^{-6} cm^2 s^{-1}]	x_h [nm]	$\rho_{particle}$ [g cm^{-3}]	x_c [nm]	d_{shell} [nm]
Feed	11.35 ± 0.66	1.81 ± 0.10	4.38 ± 0.23	1.453 ± 0.029	2.35 ± 0.09	1.01 ± 0.07
Fraction #1	10.78 ± 0.07	1.78 ± 0.02	4.44 ± 0.04	1.407 ± 0.006	2.33 ± 0.01	1.05 ± 0.01
Fraction #2	6.96 ± 0.06	2.11 ± 0.01	3.75 ± 0.01	1.355 ± 0.002	1.90 ± 0.01	0.92 ± 0.00
Fraction #3	64.50 ± 16.23	0.58 ± 0.02	13.65 ± 0.50	1.211 ± 0.112	—	—

 This journal is © The Royal Society of Chemistry 2015

Published on 25 September 2015. Downloaded by Pennsylvania State University on 16/09/2016 06:11:00.

This can be explained by removal of a small amount of stabilizer during SSP. Slight variations of x_h, d_{shell} and x_c for the feed and fraction #1 can be explained by larger structures (*e.g.* aggregates), which were still present in the feed but removed during the first steps of SSP. This is also supported by the higher standard deviation for the data of the feed. Comparing these values to literature data which predict a slightly higher value of 1.5 nm for 1-DDT bound on a gold surface – derived for an estimated molecule length of 1.7 nm[46,53] bound to the surface by an angle of 30°[54] – 1 nm seems to be quite reasonable as surface binding distances and interactions between molecule chains on QDs will certainly differ from those values obtained for bulk crystals. When calculating x_c from x_h and d_{shell}, values exceeding from 1.90 nm (fraction #2) to 2.35 nm (feed) are obtained.

Moreover, we compared our results obtained by AUC to the data found by TGA as an independent validation. Taking the data from the 2-dimensional evaluation and assuming the density of the shell to be in the range of the solvent density (density of 1-DDT is 0.845 g cm^{-3}), a mass fraction of the shell of 51.4 wt% is obtained for coarse fraction #1. In comparison, the TGA measurement gave a mass fraction of the shell of 45.6 wt% (Table 1), which is in good agreement to the data from the AUC measurements. A slightly lower value of the mass fraction resulting from TGA is reasonable because some of the solvent molecules attached to the stabilizing layer get easily lost when drying the powder before performing the TGA experiments. The results for fines fraction #2, which were found to be 54.2 wt% for AUC and 53.3 wt% for TGA, respectively, match very well. The very low density of fraction #3 (1.211 g cm^{-3}) indicates that a thick shell of stabilizer molecules must be bound to the QDs, which is also confirmed by the TGA measurements. Hence, these results demonstrate the excellent consistency of these fundamentally different techniques, namely AUC, TEM and TGA.

To further assess the sedimentation coefficient distributions of the different fractions with higher resolution, we carried out $c(s)$ analyses. The results of the $c(s)$ analyses are presented in Fig. 3. As expected from the $c(s,D)$ analyses, the distributions of the feed and fraction #1 are very similar. A slight difference is observed at the lower end of the sedimentation coefficient distribution (highlighted by arrow #1), since smallest species which were present in the feed material are no more present in fraction #1. Moreover, a small amount of faster sedimenting species is found in the feed but not in fraction #1 anymore (highlighted by arrow #2). As discussed beforehand, we attribute this to loose agglomerates, which might be formed due to the higher concentration of stabilizer in the feed and which are lost or destroyed during SSP. As shown *via* $c(s,D)$, species with a much smaller sedimentation coefficient and hence smaller particle sizes are found in fraction #2. A slight shoulder resembling medium sized particles similar to the feed is further observed. This explains the second species in $c(s,D)$ analysis (Fig. S2c†).

Based on the minimum and maximum sedimentation coefficients found for the feed, the lower and upper limit of

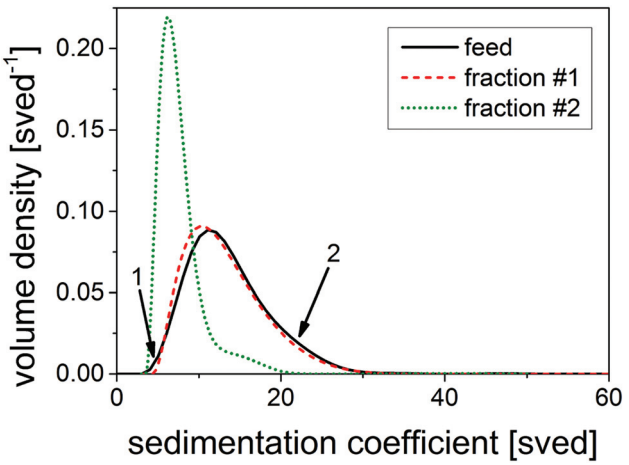

Fig. 3 Sedimentation coefficient distributions of the feed (black line), coarse fraction #1 (red dashed line) and fines fractions #2 (green dotted line) as obtained by c(s) analysis at 360 nm. Herein, it is assumed that the mass-related extinction coefficient is independent of the particle size at the wavelength used for evaluation. This results in a volume weighted distribution.

the core diameter distribution as obtained by AUC can be determined, which is 1.5 nm and 3.8 nm, respectively. This fits the results from TEM and SAED analysis, which found QDs with core diameters between ~1.4 nm and ~3.0 nm. We expect that larger QDs are found by AUC due to its superior statistics. A detection of larger structures by TEM is impeded due to their comparably low concentration (see Fig. 5 and tailing of the distribution at the upper end).

Concluding, by means of the AUC analysis we could resolve the core–shell structure of the $CuInS_2$ QDs after the SSP process directly in solution. The mean core diameters of the feed, fraction #1 and fraction #2 were found to be 2.35 nm, 2.33 nm and 1.9 nm, respectively. A shell thickness of about 1 nm was further derived by the 2-dimensional analysis. The range of core diameters found by AUC (1.5 nm < x_c < 3.8 nm) is in good agreement with the results obtained by TEM and SAED for a finite number of NPs (mean values: 1.4 nm and 3.0 nm) and XRD (mean values: 2.4 nm and 2.9 nm). Congruence of the values obtained with different methods is not expected and not possible due to various reasons. While AUC gives information on hydrodynamic diameters and particle densities for all particles in the sample which then can be converted into core sizes based on a mass conservation approach, HRTEM is capable to give information about single particles. SAED and XRD in contrast give mean values for a certain amount of particles. Nevertheless, the size range between 1.5 nm and 3.8 nm is relatively narrow. Even more important with respect to SSP, our AUC analysis reveals that SSP of the $CuInS_2$ QDs results in an enrichment of larger species in fraction #1 and an enrichment of smaller species in fraction #2. The information on the QD shells in the single fractions, which was derived by the particle densities obtained by the 2-dimensional analysis are in excellent agreement to the TGA

Published on 25 September 2015. Downloaded by Pennsylvania State University on 16/09/2016 06:11:00.

results, *i.e.*, showing an increased relative organic surrounding of smaller QDs. The residuals fraction #3 investigated by means of AUC revealed much larger species with small density, which must be assigned to agglomerates containing a lot of stabilizer, again confirming the TGA results.

3.5. Optical properties of $CuInS_2$ QDs after SSP

Having confirmed the existence of $CuInS_2$ QDs with tetragonal crystal structure and sizes ranging from 1.5 to 3.8 nm in the feed sample, optical characteristics shall be analyzed in the following. First, a bandgap *vs.* size dependency shall be established by calibration of PSD calculation results against AUC data. This allows the derivation of consistent PSDs by deconvolution of absorbance spectra, then followed by analysis of the emission of the single fractions.

3.5.1. Bandgap *vs.* size relationship. In order to confirm the core–shell model applied to evaluate the AUC core data and, thus, to further validate our results, we used the core distributions of fractions #1 and #2 to determine the bandgap *vs.* size dependency of $CuInS_2$. Analogue to previous studies,[33] a power law with three parameters (a = 2.0301 nm, b = −0.649 and c = 0 nm) was used to describe the correlation between particle size and bandgap energy according to eqn (5) (see Experimental section for details).

Fig. 4 shows the comparison of $\Delta E(x)$ obtained by us with experimental data using absorption and 2-dimensional photoluminescence excitation (PLE) spectra according to Zhong *et al.*[55] as well as an EMA reported by Omata *et al.*[56] To the best of our knowledge, this is the only data available on the bandgap *vs.* size relationship of $CuInS_2$ QDs. We assign this limitation in data availability – at least in comparison to Pb- or Cd-based QD systems – to the aforementioned issues with proper size determination by HRTEM and the novelty of $CuInS_2$ QDs.

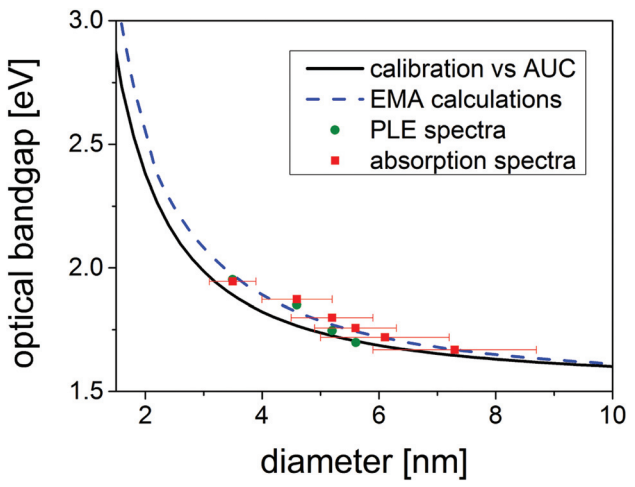

Fig. 4 Comparison of size-dependent optical bandgap of $CuInS_2$ NCs from calibration *vs.* AUC (black line), EMA calculations[56] (blue dashed line), absorption spectra[55] (red squares) and PLE spectra[55] (green spheres). Tabulated values are summarized in Table S3 in ESI.†

First, we compare the experimentally derived $\Delta E(x)$ curves from absorption, PLE and AUC (the data derived from calibration *vs.* AUC is additionally given in Table S3, ESI†). Notably, the literature studies were performed on particles with sizes between 3 nm and 8 nm, thus, particles with sizes mainly larger than 4 nm, whereas the QDs discussed herein are situated well below 4 nm. The highest accuracy of eqn (5) within our study is expected for the investigated size range below 4 nm. Nevertheless, the extrapolated values for sizes above 4 nm match well with the experimental findings. Further comparing our $\Delta E(x)$ with the EMA results, a good coincidence for larger particles is observed whereas eqn (6) leads to smaller bandgap energies for sizes below ~6 nm. Such a shift is expected as EMA usually overestimates the bandgap of small particles with strong quantum confinement. However, in comparison to other QD materials like ZnO[57] or CdS,[58] the deviation is relatively small.

Putting all this together, it becomes clear that our AUC-UV derived $\Delta E(x)$ matches the experimental reference data and is in line with our expectations regarding the comparison with EMA calculations.[57,58] This confirms once more the assumptions with respect to the shell during AUC evaluation. At this point, it needs to be mentioned that a future availability of larger particles, improved AUC analysis or a better understanding of the influence of the organic shell on the behaviour of $CuInS_2$ might lead to an improved bandgap *vs.* size correlation. However, as this work focuses on very small QDs with sizes between 1 and 4 nm, for the time being eqn (5) with parameters a–c, together with a bulk bandgap of 1.53 eV is the best description available. Thus, it will be used throughout all further calculations of $PSDs^{alg}$.

3.5.2. Deconvolution of absorbance spectra. The bandgap *vs.* size dependency derived from calibration *vs.* AUC data (Fig. 4) has been used in the following for deconvolution of absorbance spectra. In Fig. 5a, the absorbance spectrum of the feed is shown, the evaluated wavelength range for the calculation of the PSD is indicated by a blue frame (460 nm–800 nm). The spectrum in this region shows a characteristic behavior with two less distinct absorption features at ~480 nm and ~550 nm (Abs 1 and Abs 2, indicated by arrows in Fig. 5a). It has to be mentioned that data analysis of even smaller wavelengths than indicated by the blue frame would be desirable. However, in the region below 460 nm, an ongoing absorption increase of the material is noticed due to (i) higher order excitonic transitions and (ii) the absorbance of organic components. Thus, possible information on smallest nanocrystals – that are known to be present due to the fact that (i) they were identified by HRTEM, (ii) calculated from the SAED by Scherrer formula and (iii) the PSD does not reach a zero-value for small particle sizes when the minimum wavelength is fixed at 460 nm – is distorted by those additional features. However, in view of the results obtained by the formerly discussed characterization methods, we think that evaluation of wavelengths ranging from 800 nm to 460 nm and thus particle sizes down to 1.6 nm, already gives important insights to SSP. The derived PSD is shown in Fig. 5b. A slightly bimodal PSD ranging from

 This journal is © The Royal Society of Chemistry 2015

Published on 25 September 2015. Downloaded by Pennsylvania State University on 16/09/2016 06:11:00.

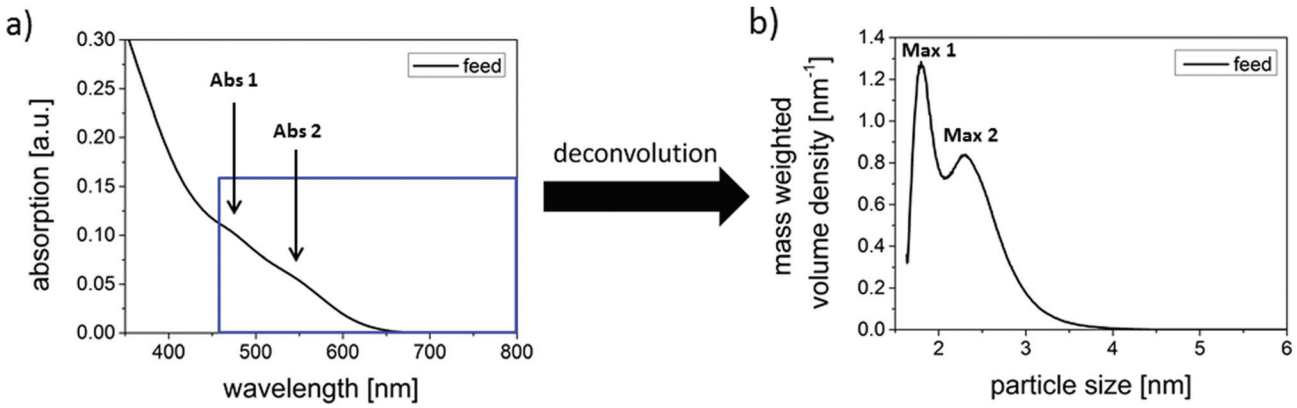

Fig. 5 (a) Absorbance spectrum of $CuInS_2$ QDs and (b) the corresponding PSD obtained by deconvolution of the wavelength range from 800 nm to 460 nm; the latter is indicated by a blue frame in the absorbance data of (a).

1.6 nm to 3.8 nm with maxima at 1.8 nm and 2.3 nm and a weak tailing at larger particle sizes between 3.0 nm and 3.8 nm was found. The bimodality results mathematically from the two features (Abs 1 and Abs 2) in the absorbance spectrum. In contrast to that, a bimodal PSD was not obtained by the AUC analysis. A possible explanation for this mismatch is the small size and the high diffusivity of the QDs which cause a broadening of the size distribution. Even though the applied $c(s)$ analysis corrects the influence of diffusion, its performance is limited due to the size dependent density of the QDs which in turn hampers the resolution of the analysis. The resolution of the 2-dimensional $c(s,D)$ analysis was also limited due to the maximum grid size of 30 × 30 points. More enhanced data analysis methods such as 2DSA[59] could not be applied due to the lack of regularization as explained in the 'theoretical background of AUC' in ESI.†

Despite the fact that particles <1.6 nm cannot be covered by the deconvolution and that the exact PSD shape cannot be unambiguously determined, the overall size range obtained is in agreement with results obtained by HRTEM, SAED, XRD and AUC. Thus, the deconvolution algorithm using the derived bandgap *vs.* size relationship is seen to be applicable for analyzing SSP of $CuInS_2$ QDs in more detail. This will be described in the following.

In Fig. 6, the absorbance spectra and the corresponding PSDs of the feed and the three isolated fractions are summarized. Regarding first the absorbance data shown in Fig. 6a, coarse fraction #1 (red dashed line) seems to be nearly identical to the absorbance of the feed (black solid line). In fines fraction #2 (green dotted line), the second absorption feature located at ~550 nm (Abs 2) is not there anymore. However, this does not mean that there is no absorption in this wavelength range at all. The onset shifted from ~675 nm to ~625 nm and the overall spectrum is narrower, however, still relatively broad if compared to the absorption of Cd-based systems. Finally, residuals fraction #3 shows a very similar absorption behavior to fines fraction #2. Noteworthy, no additional features or irregularities are present, although the sample contains a much higher amount of organic molecules than the other fractions. This indicates that the organics have no pronounced influence on the absorption behavior in the visible range, but rather link isolated QDs together without formation of solid bridges (see AUC results in section 3.4).

As shown in Fig. 6b, the calculated volume density distributions were scaled with the relative masses of the individual fractions by multiplication with c (0.90), f (0.04) and r (0.03), respectively. The values in brackets give the numbers for experiment 1 (see Table S1 in ESI†). As already expected from the absorbance spectra, the PSD of the coarse fraction #1 is almost identical to the feed distribution, showing a slightly bimodal shape with maxima at 1.8 nm and 2.3 nm. For the fines fraction #2 and the residuals fraction #3, a distribution ranging from 1.6 nm to 3.1 nm was calculated as it becomes clear from the enlargement shown in Fig. 6d. Both PSDs of fractions #2 and #3 show a single maximum located at 1.8 nm. Only a small additional feature is present around 2.1 nm. Thereby, the PSD was narrowed in terms of the total width from initially ~2.1 nm for the feed to ~1.5 nm for the fines fraction.

To verify the mass balance, the mass weighted volume densities of the three fractions #1, #2 and #3 were summed up and the deviation to the feed distribution was calculated. The result is shown in Fig. 6c by purple dotted lines. The missing part makes up 1% in the experiment exemplarily shown in Fig. 6 or 3.6% (±2.3%) when talking about mean values. The missing part mainly consists of smaller particles plus some midsized particles. According to the results discussed so far – which are congruent with AUC data – larger particles are only found in the coarse fraction. This coarse fraction makes up 90.1% of the total mass with a very small standard deviation of ±1.3%. Irrespective of the distribution of the masses amongst the other two fractions with smaller particles or the missing part, a high reproducibility for the coarse fraction is given which contains more large and less smaller particles than the feed and the other fractions. This means that 10 wt% of small particles are removed from the feed by SSP.

Published on 25 September 2015. Downloaded by Pennsylvania State University on 16/09/2016 06:11:00.

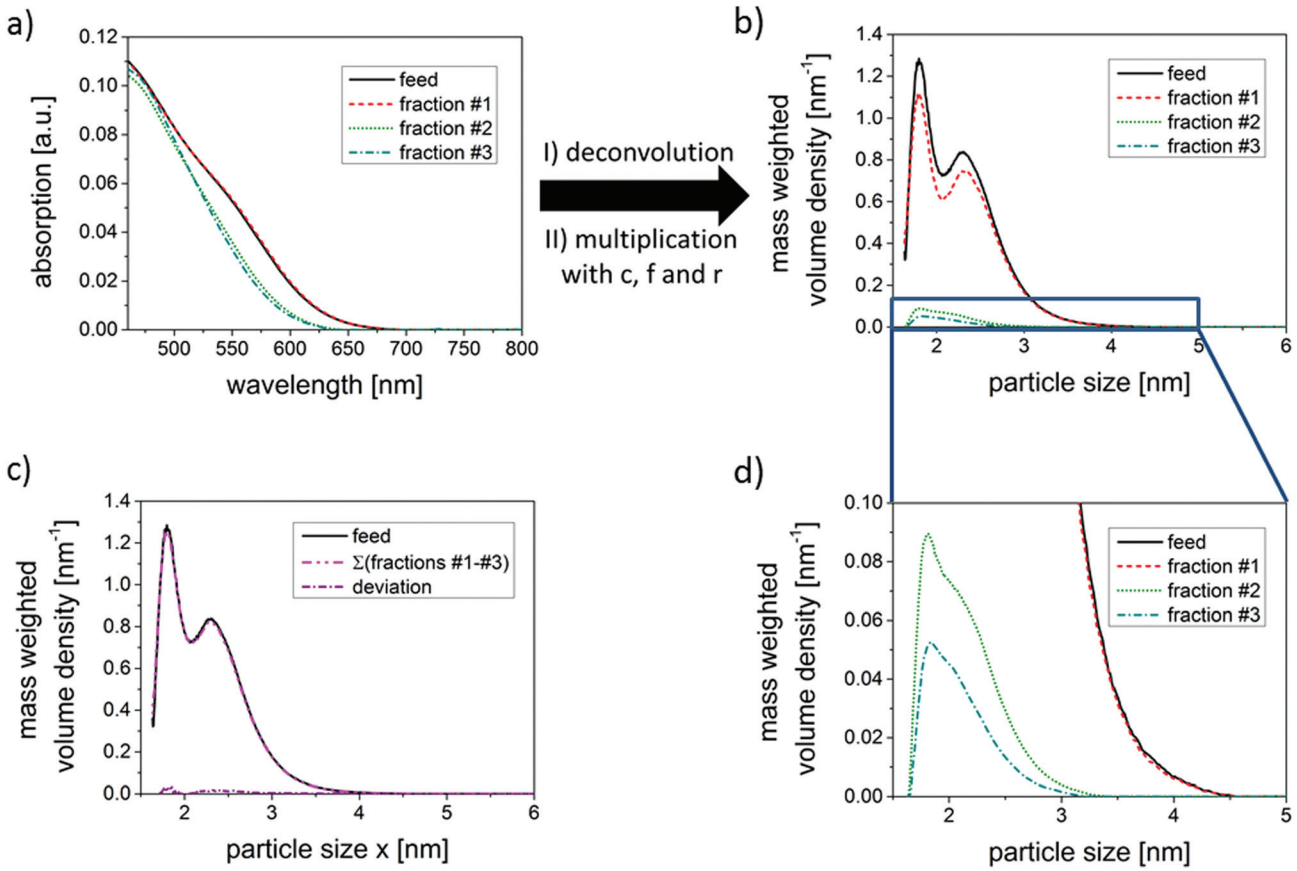

Fig. 6 (a) Absorption spectra of the feed (black solid line), coarse fraction #1 (red dashed line), fines fraction #2 (green dotted line) and residuals fraction #3 (cyan blue dashed-dotted line); (b) the therefrom derived mass weighted particle size distributions (PSD); (c) feed PSD directly derived from the absorbance measurement (black solid line) in comparison to the sum of mass weighted individual fractions #1, #2 and #3 (pink dashed line) and the deviation between the feed and the classified fractions #1, #2 and #3 (purple dotted line); (d) enlargement of fractions #2 and #3 shown in (b).

In summary, the deconvolution results show the following: the PSDs of both, feed and coarse fraction #1 are bimodal and cover a wide size range from at least 1.6 nm up to ~3.8 nm. The PSDs of the fines #2 and the residuals fractions #3 are more narrow. These findings are in agreement with the previously discussed results obtained by XRD and AUC which already indicated that these two fractions consist of clearly smaller QDs. Biggest nanocrystals with a size exceeding 3.0 nm are solely found in the coarse fraction #1 and are neither present in the fines fraction #2 nor in the residuals fraction #3. Taking further into consideration the closed mass balance by 3.6% ± 2.3%, it can be concluded that 10 wt% of medium and small particles are sorted out by SSP from the original feed PSD. Thus, large particles exceeding 3.0 nm are enriched within the coarse fraction #1.

3.4.3. Luminescence of the single fractions. Photoluminescence (PL) spectra of the samples are shown in Fig. 7, the optical data is additionally summarized in Table S1.† Both, the feed and the coarse fraction #1 show a broad luminescence with a FWHM of about 105 nm. The emission seems to consist of two peaks with maxima at ~640 nm (Emi 1) and ~665 nm (Emi 2, indicated by black arrows) and similar relative intensities. For the fines fraction #2, however, the signal consists of one main peak which is clearly shifted to smaller wavelengths (~625 nm). Only a very small feature at ~655 nm can be identified. The FWHM of the fines fraction #2 is ~90 nm. Therefore, its emission signal is less broad than those of the feed and the coarse fraction #1. Residuals fraction #3 shows similar emission characteristics as fraction #2. So far, these results are in agreement with the absorption data, where the coarse fraction was almost identical to the feed, and a shift to smaller structures was found for the fines #2 and the residuals fraction #3.

Importantly, a further effect of SSP is the change of the emission intensity of the single fractions. Relative to the emission of the feed, the signal is increasing for coarse fraction #1 and decreasing for fines and residuals fractions #2 and #3. These results altogether hint at two important aspects:

First, the emission position for $CuInS_2$ QDs seems to be size-dependent as it is generally the case for QDs due to quantum confinement, but – to the best of our knowledge – has not yet been reported for $CuInS_2$ QDs synthesized with this method. In fraction #2 which mainly consists of smaller particles compared to fraction #1, the emission is clearly blue-shifted, which is in accordance with the larger bandgap of the

 This journal is © The Royal Society of Chemistry 2015

Published on 25 September 2015. Downloaded by Pennsylvania State University on 16/09/2016 06:11:00.

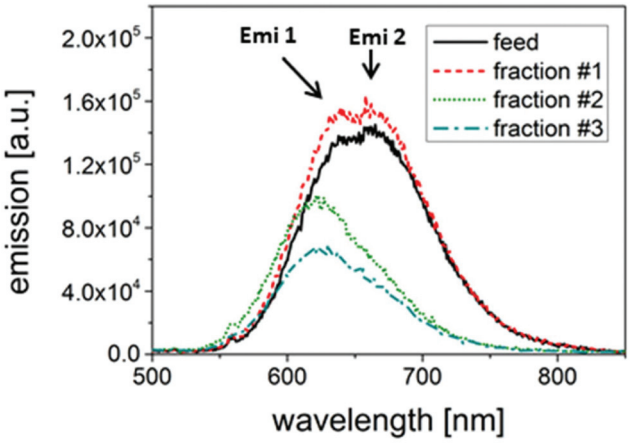

Fig. 7 Photoluminescence spectra of the feed (black solid line), the coarse fraction #1 (red dashed line), the fines fraction #2 (green dotted line) and the residuals fraction #3 (cyan blue dashed-dotted line). All samples were diluted to an optical density of 0.1 at 480 nm, the excitation wavelength was λ_{exc} = 480 nm.

smaller nanocrystals. The small and less distinct feature at ~655 nm may be ascribed to particles with medium sizes. Furthermore, the FWHM of fraction #2 is narrower, which may result from the fact that a smaller range of particle sizes is contributing to the emission. The emission properties of multicomponent QDs have been investigated in the past[60–63] with a focus on the underlying recombination mechanisms. The position of the emission signal in $CuInS_2$-based systems has been attributed to donor–acceptor pair (DAP) recombinations on the surface (higher energy) or inside the particles (lower energy).[46,60] Our investigations show a size-dependency of the luminescence position which is most likely in agreement with a location dependent mechanism. As smaller particles have a comparably larger surface-to-volume ratio, the probability of recombination to occur *via* surface processes will ineluctably be increased. For larger particles, instead, the relative probability for a DAP to happen within the particle might be enhanced. Future emission lifetime measurements could shed further light on the optical properties of the single size fractions of $CuInS_2$ QDs.

Second, larger nanocrystals seem to emit stronger than smaller ones. This effect was also reported for the classification of Si nanocrystals[64] and Mn-doped ZnS nanoparticles.[65] To recheck whether the increased luminescence results from a real size effect or from the washing itself (note that the additional classification of coarse fraction #1 might change the particle surface in comparison to the feed), two tests were performed: in one experiment, the purification step of the feed was repeated once more, *i.e.*, an excess of antisolvent was added and centrifugation was performed (for purification details see Experimental section). In another experiment, all separated fractions were mixed back together after SSP. For both tests, optical characterization of the newly-prepared samples was performed. A schematic illustration of the two experiments and the corresponding spectra is shown in Scheme S2 and Fig. S3 in ESI,† respectively. The results were the following: (i) the absorption spectra of the samples obtained from both experiments were identical to the absorption of the feed discussed previously. (ii) The shape of the luminescence signal in both cases was identical to the one of the feed as well. (iii) However, the intensity of the luminescence signal did not increase (as it did for fraction #1), but decreased slightly in both cases, a further washing step as well as recombination of the separated fractions after SSP. The latter proves that each purification step and therefore removal of protective surface ligands leads to a decrease in PL intensity for $CuInS_2$ nanocrystals (see ESI† 'additional experiments' for detailed discussion of the tests and the interpretation of the results).

Therefore, we can clearly rule out washing effects as a reason for the increase of PL intensity. Instead, especially the second experiment, in which already separated fractions were recombined, proves the size effect to be the main reason for the increase in emission intensity. We assume that the reduced emission of smaller QDs (fractions #2 and #3) is due to their higher surface-to-volume ratio that leads to an increased impact of surface defects, causing a quenching of the emission. Fraction #1 in turn shows an improved emission in comparison to the feed although it has undergone one washing step (or at least a procedure that is very similar to washing) more than the feed. It contains the highest relative amount of larger nanocrystals where surface defects and the relative amount of organics are reduced. This leads to less quenching. Thus, a selective reduction of the mass of smaller nanocrystals in a given feed sample by only 10% (relative mass of fraction #2 plus #3 referred to the total mass of $CuInS_2$ QDs) leads to an improvement in the emission properties. This finding evidences the strong influence of smallest changes in a QD PSD with respect to the later product properties.

4. Conclusion

In this study, the influence of the PSD on the optical properties of $CuInS_2$ QDs was investigated. HRTEM and SAED depicted the existence of particles with sizes ranging from at least 1.4 nm to 3 nm. By means of AUC analysis a core size distribution ranging from 1.5 nm to 3.8 nm was obtained. Regarding the small deviation between the AUC and SAED size measurements, it has to be stated that the latter just provides a mean size of a small fraction of the particles present in the sample, while AUC delivers information on the PSD of the whole ensemble. This PSD data (PSD^{AUC}) was used in a next step together with PSDs obtained by deconvolution of absorbance data (PSD^{alg}) to derive a bandgap *vs.* particle size relationship. While deconvolution of the absorption spectra led to a slightly bimodal PSD of the feed sample, a monomodal core size distribution was obtained by AUC possibly due to a broadening of the distribution caused by the small size of the QDs and their diffusivity. The correction for these factors

Published on 25 September 2015. Downloaded by Pennsylvania State University on 16/09/2016 06:11:00.

is an ongoing process which was already solved for more simple systems[39] and might be solved for $CuInS_2$ QDs in the near future as well. The particle sizes obtained by deconvolution of absorbance spectra were ranging from 1.6 nm up to 3.8 nm. Smaller particle sizes could not be extracted from the absorption spectrum due to an overlapping of size information with other features, mainly resulting from excitonic states and organic molecules.

SSP was performed to classify the nanocrystals. Detailed characterization of the starting feed material and the final fractions revealed the structural and compositional homogeneity of the particle cores in the single fractions. The obtained mean sizes generally are in agreement within 1 Å, *i.e.* 2.3 nm for the coarse fraction #1 by both AUC and deconvolution of the absorbance spectrum; and mean sizes of 1.9 nm (AUC) and 1.8 nm (deconvolution) for the fines fraction #2. Thus, SSP resulted in the separation of smaller particles from the larger particles. The influence of SSP on the optical performance was investigated and revealed that differences in the spectra can be mainly attributed to size effects. We could show that optical characteristics as absorption and emission features as well as their positions are influenced by the particle sizes present in the sample. Moreover, our results show that the relatively broad FWHM of the PL signal of $CuInS_2$ QDs is at least partly related to the underlying width of the PSD. To the best of our knowledge, the reason for this typical broad emission signal which is usually observed for multicomponent materials was not explained before. Furthermore, a removal of 10% of the samples' total mass on smallest particles leads to an increase of the emission intensity. This is ascribed to the preferential sorting out of small particles which have a higher surface-to-volume ratio and a relatively defect-rich surface.

It is important to point out that this work focuses on the effect of the PSD. Further factors, *e.g.* identity of organic surface ligands, bonding nature, ligand coverage, and most important, the influence of these factors on the electronic states, will certainly have an additional influence on the emission properties. As the surface coverage and nature of ligands is influencing the SSP as well, detailed investigation of the interface characteristics is expected to result in better separation efficiencies in future. Our work is aimed to provide an insight into the effect of the PSD on optical characteristics by using the simple but not yet in detail understood approach SSP. We are fairly convinced that improved synthesis and post-processing will result in more defined and better controllable emission characteristics for multicomponent QD systems in future.

Acknowledgements

The authors would like to thank the German Research Council (DFG) for financial support within the framework of its Excellence Initiative the Cluster of Excellence "Engineering of Advanced Materials" (DFG EXC 315). Additionally, we would like to thank Bayer Technology Services (BTS) for financial support. B. W. gratefully acknowledges the Research Training Group "Disperse Systems for Electronic Applications" (GRK 1161). Furthermore, J. W. thanks the DFG for financial support through project "PE 427/28-1". T. A. is deeply grateful to P. Hoppe for ICP-OES measurements at the Institute of Particle Technology (LFG, Friedrich-Alexander-Universität Erlangen-Nürnberg).

References

1 K. L. Kelly, E. Coronado, L. L. Zhao and G. C. Schatz, The optical properties of metal nanoparticles: The influence of size, shape, and dielectric environment, *J. Phys. Chem. B*, 2003, **107**(3), 668–677.
2 R. W. Murray, Nanoelectrochemistry: metal nanoparticles, nanoelectrodes, and nanopores, *Chem. Rev.*, 2008, **108**(7), 2688–2720.
3 M. C. Daniel and D. Astruc, Gold nanoparticles: assembly, supramolecular chemistry, quantum-size-related properties, and applications toward biology, catalysis, and nanotechnology, *Chem. Rev.*, 2004, **104**(1), 293–346.
4 M. Hu, J. Chen, Z.-Y. Li, L. Au, G. V. Hartland, X. Li, M. Marquez and Y. Xia, Gold nanostructures: engineering their plasmonic properties for biomedical applications, *Chem. Soc. Rev.*, 2006, **35**(11), 1084–1094.
5 V. I. Klimov, *Semiconductor and metal nanocrystals: synthesis and electronic and optical properties*, CRC Press, 2003, p. 500.
6 B. L. Cushing, V. L. Kolesnichenko and C. J. O'Connor, Recent advances in the liquid-phase syntheses of inorganic nanoparticles, *Chem. Rev.*, 2004, **104**(9), 3893–3946.
7 M. Afzaal and P. O'Brien, Recent developments in II-VI and III-VI semiconductors and their applications in solar cells, *J. Mater. Chem.*, 2006, **16**(17), 1597–1602.
8 K. Grieve, P. Mulvaney and F. Grieser, Synthesis and electronic properties of semiconductor nanoparticles/quantum dots, *Curr. Opin. Colloid Interface Sci.*, 2000, **5**(1–2), 168–172.
9 S. Kumar and T. Nann, Shape control of II-VI semiconductor nanomateriats, *Small*, 2006, **2**(3), 316–329.
10 M. J. Anc, N. L. Pickett, N. C. Gresty, J. A. Harris and K. C. Mishra, Progress in non-Cd quantum dot development for lighting applications, *ECS J. Solid State Sci. Technol.*, 2013, **2**(2), R3071–R3082.
11 D. R. Lide, *Handbook of Chemistry and Physics*, CRC Press Inc, 84th edn, 2004.
12 H. Neumann, W. Horig, V. Savelev, J. Lagzdonis, B. Schumann and G. Kuhn, The optical-properties of CuInS2 thin-films, *Thin Solid Films*, 1981, **79**(2), 167–171.
13 M. Kanzari and B. Rezig, Effect of deposition temperature on the optical and structural properties of as-deposited CuInS2 films, *Semicond. Sci. Technol.*, 2000, **15**(4), 335–340.
14 D. Zhitomirsky, I. J. Kramer, A. J. Labelle, A. Fischer, R. Debnath, J. Pan, O. M. Bakr and E. H. Sargent, Colloidal quantum dot photovoltaics: the effect of polydispersity, *Nano Lett.*, 2012, **12**(2), 1007–1012.

 This journal is © The Royal Society of Chemistry 2015

Published on 25 September 2015. Downloaded by Pennsylvania State University on 16/09/2016 06:11:00.

15 V. I. Klimov, A. A. Mikhailovsky, S. Xu, A. Malko, J. A. Hollingsworth, C. A. Leatherdale, H. J. Eisler and M. G. Bawendi, Optical gain and stimulated emission in nanocrystal quantum dots, *Science*, 2000, **290**(5490), 314–317.
16 S. Coe, W. K. Woo, M. Bawendi and V. Bulovic, Electroluminescence from single monolayers of nanocrystals in molecular organic devices, *Nature*, 2002, **420**(6917), 800–803.
17 A. Eychmuller, L. Katsikas and H. Weller, Photochemistry of semiconductor colloids.35. Size seperation of colloidal CdS by gel-electrophoresis, *Langmuir*, 1990, **6**(10), 1605–1608.
18 X. T. Song, L. Li, H. F. Chan, N. H. Fang and J. C. Ren, Highly efficient size separation of CdTe quantum dots by capillary gel electrophoresis using polymer solution as sieving medium, *Electrophoresis*, 2006, **27**(7), 1341–1346.
19 C. H. Fischer, H. Weller, L. Katsikas and A. Henglein, Photochemistry of colloidal semiconductors .30. HPLC investigation of small CdS particles, *Langmuir*, 1989, **5**(2), 429–432.
20 J. H. Fendler, Atomic and molecular clusters in membrane mimetic chemistry, *Chem. Rev.*, 1987, **87**(5), 877–899.
21 C. B. Murray, D. J. Norris and M. G. Bawendi, Synthesis and characterization of nearly monodisperse CdE (E = S, SE, TE) semiconductor nanocrystallites, *J. Am. Chem. Soc.*, 1993, **115**(19), 8706–8715.
22 A. Chemseddine and H. Weller, Highly monodisperse quantum sized CdS particles by size-selective precipitation, *Ber. Bunsen-Ges.-Physical Chemistry Chemical Physics*, 1993, **97**(4), 636–637.
23 T. Vossmeyer, L. Katsikas, M. Giersig, I. G. Popovic, K. Diesner, A. Chemseddine, A. Eychmuller and H. Weller, CdS nanoclusters - synthesis, characterization, size-dependent oscillator strength, temperature shift of the excitonic-transition energy, and reversible absorbence shift, *J. Phys. Chem.*, 1994, **98**(31), 7665–7673.
24 M. Baalousha and J. R. Lead, Size fractionation and characterization of natural aquatic colloids and nanoparticles, *Sci. Total Environ.*, 2007, **386**(1–3), 93–102.
25 M. Baalousha and J. R. Lead, Characterization of natural aquatic colloids (< 5 nm) by flow-field flow fractionation and atomic force microscopy, *Environ. Sci. Technol.*, 2007, **41**(4), 1111–1117.
26 L. Calzolai, D. Gilliland, C. P. Garcia and F. Rossi, Separation and characterization of gold nanoparticle mixtures by flow-field-flow fractionation, *J. Chromatogr., A*, 2011, **1218**(27), 4234–4239.
27 B. Kowalczyk, I. Lagzi and B. A. Grzybowski, Nanoseparations: strategies for size and/or shape-selective purification of nanoparticles, *Curr. Opin. Colloid Interface Sci.*, 2011, **16**(2), 135–148.
28 Y. Mori, Size-selective separation techniques for nanoparticles in liquid, *KONA powder and particle journal*, 2015, **32**, 102–114.
29 S. L. Castro, S. G. Bailey, R. P. Raffaelle, K. K. Banger and A. F. Hepp, Synthesis and characterization of colloidal CuInS2 nanoparticles from a molecular single-source precursor, *J. Phys. Chem. B*, 2004, **108**(33), 12429–12435.
30 L. Li, T. J. Daou, I. Texier, C. Tran Thi Kim, L. Nguyen Quang and P. Reiss, Highly luminescent CuInS2/ZnS core/shell nanocrystals: cadmium-free quantum dots for in vivo imaging, *Chem. Mater.*, 2009, **21**(12), 2422–2429.
31 W. Zhang and X. Zhong, Facile synthesis of ZnS-CuInS2-alloyed nanocrystals for a color-tunable fluorchrome and photocatalyst, *Inorg. Chem.*, 2011, **50**(9), 4065–4072.
32 D. Segets, J. Gradl, R. K. Taylor, V. Vassilev and W. Peukert, Analysis of optical absorbance spectra for the determination of ZnO nanoparticle size distribution, solubility, and surface energy, *ACS Nano*, 2009, **3**(7), 1703–1710.
33 D. Segets, J. M. Lucas, R. N. K. Taylor, M. Scheele, H. Zheng, A. P. Alivisatos and W. Peukert, Determination of the quantum dot band gap dependence on particle size from optical absorbance and transmission electron microscopy measurements, *ACS Nano*, 2012, **6**(10), 9021–9032.
34 D. Segets, S. Komada, B. Butz, E. Spiecker, Y. Mori and W. Peukert, Quantitative evaluation of size selective precipitation of Mn-doped ZnS quantum dots by size distributions calculated from UV/Vis absorbance spectra, *J. Nanopart. Res.*, 2013, **15**(4), 1486.
35 T. Akdas, M. Distaso, S. Kuhri, B. Winter, B. Birajdar, E. Spiecker, D. M. Guldi and W. Peukert, The effects of post-processing on the surface and the optical properties of copper indium sulfide quantum dots, *J. Colloid Interface Sci.*, 2015, **445**, 337–347.
36 H. M. Strauss, E. Karabudak, S. Bhattacharyya, A. Kretzschmar, W. Wohlleben and H. Cölfen, Performance of a Fast Fiber Based UV/Vis Multiwavelength Detector for the Analytical Ultracentrifuge, *Colloid Polym. Sci.*, 2008, **286**(2), 121–128.
37 J. Walter, K. Löhr, E. Karabudak, W. Reis, J. Mikhael, W. Peukert, W. Wohlleben and H. Cölfen, Multidimensional Analysis of Nanoparticles with Highly Disperse Properties Using Multiwavelength Analytical Ultracentrifugation, *ACS Nano*, 2014, **8**(9), 8871–8886.
38 H. M. Pathan and C. D. Lokhande, Chemical deposition and characterization of copper indium disulphide thin films, *Appl. Surf. Sci.*, 2004, **239**(1), 11–18.
39 P. Schuck, Size-distribution analysis of macromolecules by sedimentation velocity ultracentrifugation and Lamm equation modeling, *Biophys. J.*, 2000, **78**(3), 1606–1619.
40 P. Schuck, Sedimentation analysis of noninteracting and self-associating solutes using numerical solutions to the Lamm equation, *Biophys. J.*, 1998, **75**(3), 1503–1512.
41 P. H. Brown and P. Schuck, Macromolecular size-and-shape distributions by sedimentation velocity analytical ultracentrifugation, *Biophys. J.*, 2006, **90**(12), 4651–4661.
42 N. S. Pesika, K. J. Stebe and P. C. Searson, Relationship between absorbance spectra and particle size distributions for quantum-sized nanocrystals, *J. Phys. Chem. B*, 2003, **107**(38), 10412–10415.
43 N. S. Pesika, K. J. Stebe and P. C. Searson, Determination of the particle size distribution of quantum nanocrystals from absorbance spectra, *Adv. Mater.*, 2003, **15**(15), 1289–1291.

Published on 25 September 2015. Downloaded by Pennsylvania State University on 16/09/2016 06:11:00.

44 R. Viswanatha and D. D. Sarma, Study of the growth of capped ZnO nanocrystals: A route to rational synthesis, *Chem. – Eur. J.*, 2006, **12**(1), 180–186.
45 O. I. Mićić, C. J. Curtis, K. M. Jones, J. R. Sprague and A. J. Nozik, Synthesis and characterization of InP quantum dots, *J. Phys. Chem.*, 1994, **98**(19), 4966–4969.
46 M. I. Alonso, K. Wakita, J. Pascual, M. Garriga and N. Yamamoto, Optical functions and electronic structure of CuInSe2, CuGaSe2, CuInS2, and CuGaS2, *Phys. Rev. B: Condens. Matter*, 2001, **63**(7), 075203.
47 H. Zhong, Y. Zhou, M. Ye, Y. He, J. Ye, C. He, C. Yang and Y. Li, Controlled synthesis and optical properties of colloidal ternary chalcogenide CuInS2 nanocrystals, *Chem. Mater.*, 2008, **20**(20), 6434–6443.
48 S. C. Abrahams and J. L. Bernstein, Piezoelectric nonlinear optic CuGaS2 and CuInS2 crystal structure: Sublattice distortion in AIBIIIC2VI and AIIBIVC2 V type chalcopyrites, *J. Chem. Phys.*, 1973, **59**, 5415–5420.
49 E. E. Lees, M. J. Gunzburg, T.-L. Nguyen, G. J. Howlett, J. Rothacker, E. C. Nice, A. H. A. Clayton and P. Mulvaney, Experimental determination of quantum dot size distributions, ligand packing densities, and bioconjugation using analytical ultracentrifugation, *Nano Lett.*, 2008, **8**(9), 2883–2890.
50 H. Cölfen and T. Pauck, Determination of Particle Size Distributions With Angström Resolution, *Colloid Polym. Sci.*, 1997, **275**(2), 175–180.
51 R. P. Carney, J. Y. Kim, H. Qian, R. Jin, H. Mehenni, F. Stellacci and O. M. Bakr, Determination of nanoparticle size distribution together with density or molecular weight by 2D analytical ultracentrifugation, *Nat. Commun.*, 2011, **2**, 335.
52 B. Demeler, T.-L. Nguyen, G. E. Gorbet, V. Schirf, E. H. Brookes, P. Mulvaney, A. a. O. El-Ballouli, J. Pan, O. M. Bakr, A. K. Demeler, B. I. Hernandez Uribe, N. Bhattarai and R. L. Whetten, Characterization of Size, Anisotropy, and Density Heterogeneity of Nanoparticles by Sedimentation Velocity, *Anal. Chem.*, 2014, **86**(15), 7688–7695.
53 M. Giersig and P. Mulvaney, Preparation of ordered colloid monolayers by electrophoretic deposition, *Langmuir*, 1993, **9**(12), 3408–3413.
54 M. D. Porter, T. B. Bright, D. L. Allara and C. E. D. Chidsey, Spontaneously organized molecular assemblies .4. Structural characterization of normal-alkyl thiol monolayers on gold by optical ellipsometry, infrared spectroscopy, and electrochemistry, *J. Am. Chem. Soc.*, 1987, **109**(12), 3559–3568.
55 H. Zhong, S. S. Lo, T. Mirkovic, Y. Li, Y. Ding, Y. Li and G. D. Scholes, Noninjection gram-scale synthesis of monodisperse pyramidal CuInS2 nanocrystals and their size-dependent properties, *ACS Nano*, 2010, **4**(9), 5253–5262.
56 T. Omata, K. Nose and S. Otsuka-Yao-Matsuo, Size dependent optical band gap of ternary I-III-VI2 semiconductor nanocrystals, *J. Appl. Phys.*, 2009, **105**(7), 073106.
57 R. Viswanatha, S. Sapra, B. Satpati, P. V. Satyam, B. N. Dev and D. D. Sarma, Understanding the quantum size effects in ZnO nanocrystals, *J. Mater. Chem.*, 2004, **14**(4), 661–668.
58 Y. Wang and N. Herron, Quantum size effects on the exciton energy of CdS clusters, *Phys. Rev. B: Condens. Matter*, 1990, **42**(11), 7253–7255.
59 E. Brookes, W. Cao and B. Demeler, A two-dimensional spectrum analysis for sedimentation velocity experiments of mixtures with heterogeneity in molecular weight and shape, *Eur. Biophys. J. Biophys. Lett.*, 2010, **39**(3), 405–414.
60 T. K. C. Tran, Q. P. Le, Q. L. Nguyen, L. Li and P. Reiss, Time-resolved photoluminescence study of CuInS2/ZnS nanocrystals, *Adv. Nat. Sci.: Nanosci. Nanotechnol.*, 2010, **1**(025007).
61 D.-E. Nam, W.-S. Song and H. Yang, Facile, air-insensitive solvothermal synthesis of emission-tunable CuInS2/ZnS quantum dots with high quantum yields, *J. Mater. Chem.*, 2011, **21**(45), 18220–18226.
62 J. S. Niezgoda, M. A. Harrison, J. R. McBride and S. J. Rosenthal, Novel synthesis of chalcopyrite CuxInyS2 quantum dots with tunable localized surface plasmon resonances, *Chem. Mater.*, 2012, **24**(16), 3294–3297.
63 M. Sakamoto, L. Chen, M. Okano, D. M. Tex, Y. Kanemitsu and T. Teranishi, Photoinduced carrier dynamics of nearly stoichiometric oleylamine-protected copper indium sulfide nanoparticles and nanodisks, *J. Phys. Chem. C*, 2015, **119**(20), 11100–11105.
64 M. L. Mastronardi, F. Maier-Flaig, D. Faulkner, E. J. Henderson, C. Kuebel, U. Lemmer and G. A. Ozin, Size-dependent absolute quantum yields for size-separated colloidally-stable silicon nanocrystals, *Nano Lett.*, 2012, **12**(1), 337–342.
65 S. Komada, T. Kobayashi, Y. Arao, K. Tsuchiya and Y. Mori, Optical properties of manganese-doped zinc sulfide nanoparticles classified by size using poor solvent, *Adv. Powder Technol.*, 2012, **23**(6), 872–877.

 This journal is © The Royal Society of Chemistry 2015